

Triple-domain Feature Learning with Frequency-aware Memory Enhancement for Moving Infrared Small Target Detection

Weiwei Duan, Luping Ji*, *Member, IEEE*, Shengjia Chen, Sicheng Zhu, Mao Ye, *Member, IEEE*

Abstract—Moving infrared small target detection presents significant challenges due to tiny target sizes and low contrast against backgrounds. Currently-existing methods primarily focus on extracting target features only from the spatial-temporal domain. For further enhancing feature representation, more information domains such as frequency are believed to be potentially valuable. To extend target feature learning, we propose a new *Triple-domain Strategy* (Tridos) with the frequency-aware memory enhancement on the spatial-temporal domain. In our scheme, it effectively detaches and enhances frequency features by a local-global frequency-aware module with Fourier transform. Inspired by the human visual system, our memory enhancement unit aims to capture the target spatial relations between video frames. Furthermore, it encodes temporal dynamics motion features via differential learning and residual enhancing. Additionally, we further design a residual compensation unit to reconcile possible cross-domain feature mismatches. To our best knowledge, our Tridos is the first work to explore target feature learning comprehensively in spatial-temporal-frequency domains. The extensive experiments on three datasets (DAUB, ITSDT-15K, and IRDST) validate that our triple-domain learning scheme could be obviously superior to state-of-the-art ones. Source codes are available at <https://github.com/UESTC-nnLab/Tridos>.

Index Terms—Moving Infrared Small Target Detection, Feature Learning, Fourier Transform, Frequency Aware, Memory Enhancement

I. INTRODUCTION

INFRARED small target detection (ISTD) has the advantages of being less negatively affected by the environment and highly resistant to external electromagnetic interference [48]. It holds significant application value in some military fields, such as maritime early warning and infrared guidance, and some civil fields, such as maritime rescue [47]. Due to the tiny size of targets, they could often lack obvious visual features and have blurred boundaries, characterized by low contrast and low signal-to-noise ratio (SNR). Consequently, accurately locating and tracking moving small targets in infrared images and videos has been a crucial and full of challenging research area in computer vision.

Over the past decades, many approaches have been proposed. From the aspect of research strategy, they could usually

*Corresponding author: Luping Ji.

This work is supported by the Aeronautical Science Foundation of China (ASFC) under Grant No. 2022Z071080006 and the National Natural Science Foundation of China (NSFC) under Grant No. 61972072.

Weiwei Duan, Luping Ji, Shenjia Chen, Sicheng Zhu and Mao Ye are with the School of Computer Science and Engineering, University of Electronic Science and Technology of China, Chengdu 611731, China (e-mail: dww@std.uestc.edu.cn; jiluping@uestc.edu.cn; shengjia-chen@std.uestc.edu.cn; sichengzhu@std.uestc.edu.cn; maoye@uestc.edu.cn)

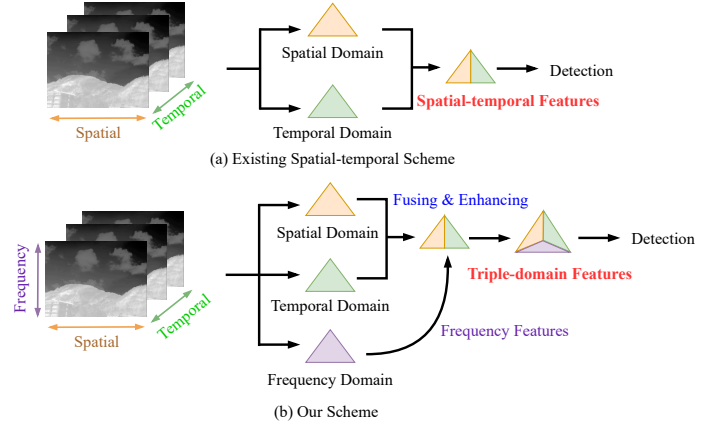


Fig. 1: The comparison between the existing spatial-temporal scheme and our scheme of triple-domain feature learning. Our scheme extract features in spatial-temporal-frequency domains.

be categorized into model-driven methods and data-driven methods [16]. Model-driven methods deeply analyze image characteristics to distinguish targets from backgrounds, often based on contrast and texture differences [1], [3]. Although these methods have achieved impressive results, they heavily depend on prior knowledge and hand-crafted features, lacking learning ability [24]. In contrast, data-driven methods have become a type of mainstream schemes in recent years [9]. They can effectively learn target detection tasks from labeled datasets [14], [15]. Therefore, our work mainly focus on the challenges faced by data-driven methods.

Furthermore, according to the different ways of using images, existing detection methods could be generally further divided into single-frame and multi-frame schemes [29]. Generally, single-frame ISTD (SISTD) does not need to consider the relations between multiple consecutive frames [12], as in [43] and [19]. These methods extract target features only from the spatial domain of images [10], owning some obvious advantages of low complexity and high detection speed. Multi-frame ISTD (MISTD) could further improve detection performance by extracting target features from both spatial and temporal domains [29], as shown in Fig. 1(a). For example, STDMA Net [30] designs a feature extractor to obtain spatial-temporal features from multi-frame consecutive images, and SSTNet [32] employs a cross-slice ConvLSTM to leverage spatial-temporal contexts also on multiple frames.

Currently, almost all MISTD methods are based on the spatial-temporal domain. They precisely capture the spatial-temporal contexts to reduce interference or enhance target features [49], [52]. Nevertheless, while these approaches are promising, they often fail to capture the intricate characteristics of small moving targets entirely. Besides, targets in intricate backgrounds could not exhibit a high correlation in consecutive frames. In these challenging situations, obtaining targets' motion details and contours is extremely difficult, decreasing the detection performance. The information from different domains is complementary, which helps to characterize the target features more comprehensively. Therefore, it is compelling to introduce more information domains in feature learning.

Consequently, a vital issue for MISTD is capturing fine-grained target features without being affected by complex scenarios. Many image processing studies [51], [50] have shown that frequency domain features provide information at different frequencies. Frequency information is potentially valuable because, in the frequency domain, noise is usually distributed at higher frequencies, while targets are distributed at lower frequencies. Frequency domain processing could reduce noise disturbance, effectively improving the accuracy of ISTD. Inspired by these findings, we develop a new triple-domain feature learning scheme to integrate the frequency domain into the existing spatial-temporal domain, as shown in Fig. 1(b). However, further exploration is needed to effectively acquire and integrate features from both spatial-temporal and frequency domains simultaneously.

To effectively tackle the challenges above, we propose a new *Triple-domain Strategy (Tridos)* of frequency-aware memory enhancement for further enhancing target feature learning. It is dedicated to exploiting the potential of frequency information, enhancing target representation comprehensively. Our scheme concentrates on depicting targets in spatial-temporal-frequency domains, exploiting their dynamic variations in the frequency domain for promoting detection performance. It is the first time to model the task of MISTD from a frequency-aware spatial-temporal perspective. In summary, the main contributions are summarized as follows:

(I) We explore and propose **Tridos**, a pioneering triple-domain scheme to extend the feature learning perspective for MISTD. Besides traditional spatial-temporal domains, it can capture target features from the frequency domain and then realize the fusion and enhancement of spatial-temporal-frequency features.

(II) Based on the Fourier transform, a local-global frequency-aware module (LGFm) is developed to extract comprehensive frequency features from local and global perceptual patterns. Moreover, inspired by the human visual system, a memory-enhanced spatial relationship module (MSRM) is designed to model the inter-frame correlations of small targets.

(III) A residual compensation unit (RCU) is constructed to eliminate the possible feature mismatches between cross-different domains, then auxiliarily fuse & enhance spatial-temporal-frequency features of small targets.

(IV) By improving popular IoU loss, a new dual-view regression loss function, especially for infrared small target detection, is defined to optimize model training.

II. RELATED WORK

A. Single-frame Infrared Small Target Detection

Single-frame infrared small target detection deals with stationary targets in a single image, which can be divided into model-driven and data-driven methods.

Model-driven methods extract tiny targets by exploiting the characteristics of the image for target enhancement or background suppression, followed by threshold segmentation [53]. They can be further categorized into filter-based, human visual system (HVS)-based, and data structure-based methods. Filter-based methods utilize the difference between target and background pixels to highlight targets and remove background noise interference, such as Top-hat [1] and Maxmean [2]. HVS-based methods extract salient regions by measuring the maximum contrast between the center pixel and neighboring regions, such as local contrast measure (LCM) [3] and its modified version: RLCM [4], HBMLCM [5], and WSLCM [6]. Data structure-based methods employ the structure of infrared images to separate the background and the target, such as IPI [7] and SMSL [8]. Although these model-driven approaches have achieved outstanding performance, they cannot adapt to intricate environments.

Data-driven methods primarily exploit deep neural networks that can adaptively learn target features by training on many training samples. They become dominant with the availability of small infrared target detection datasets [9], [12], [10]. For example, ACMNet [9] integrates low-level details and high-level semantics through asymmetric contextual modulation, and they further introduce dilated local contrast measurements in ALCNet [13]. DNANet [12] designs a dense nested interactive network to enhance the features of small targets. Moreover, AGPCNet [14] develops an attention-guided pyramid context network to obtain a global association of semantics. RDIAN [15] uses multi-scale convolutions to capture diverse target features and extend the receptive field. UIUNet [17] integrates two U-nets to learn the multi-scale and multi-level representations. ISNet [10] creatively emphasizes the importance of target shape. Furthermore, EFLNet [18] constructs a feature-enhancing learning network. RPCANet [19] proposes an interpretable deep neural network with theory-guided to replace matrix computation.

Single-frame infrared small target detection has been widely studied and has performed well. However, this pipeline ignores the motion features of targets. It is susceptible to noise and background interference, especially in challenging scenarios.

B. Multi-frame Infrared Small Target Detection

In contrast, multi-frame schemes process multiple consecutive frames simultaneously. Therefore, extracting the spatial-temporal features of targets has received extensive attention.

In terms of the traditional schemes, optical flow-based methods [21], [20] utilize brightness variations in different frames to describe target motion features. STCP [21] employs the optical flow algorithm to compute the dense trajectory of targets and then creates a binary image to extract salient contours as candidate target regions. Some methods construct spatial-temporal tensors to distinguish targets from

backgrounds, such as 4D STT [22] and NPSTT [24]. To solve the issue of inaccurate background estimation, NTLA [25] proposes a nonconvex tensor low-order approximation strategy. FST-FLNN [23] improves tensor nuclear norm using log operation for target enhancement and background suppression. Moreover, energy accumulation-based methods [26], [27] can effectively improve the SNR and enhance the energy of small targets. The dynamic programming-based methods [28] search for the optimal motion trajectory of targets through the dynamic programming algorithm. Although these traditional methods have made some progress, they rely heavily on prior knowledge.

To overcome the problems of the traditional methods above, some approaches apply deep learning to MISTD. This pipeline can exploit the temporal association between sequential frames to improve detection performance. However, it has yet to be entirely explored due to the lack of adequate MISTD datasets with high-quality annotations. The most representative methods are as follows. For instance, the interframe energy accumulation enhancement method is proposed in [29] to enhance small targets. STDManet [30] introduces a spatial-temporal differential multiscale attention network. It is the first study to introduce a temporal attention mechanism for MISTD. DTUM [31] is proposed to encode motion direction and thus extract motion information. Moreover, SSTNet [32] designs a sliced spatial-temporal network to employ cross-slice motion context. Recently, ST-Trans [33] introduces a spatial-temporal transformer to learn the associations between consecutive frames to handle complex scenarios. However, these methods only consider effectively extracting and exploiting target features from the spatial-temporal domain and scarcely consider the utilization of frequency information implied in consecutive frames.

Therefore, in this work, we focus on applying the frequency-domain information of sequential frames to traditional spatial-temporal networks, enhancing target feature learning. Furthermore, referencing available repositories, we construct a new MISTD dataset (ITSdT-15K) with accurate bounding box annotations to additionally validate our proposed method on MISTD. Their details are in section IV.

III. METHODOLOGY

A. Overall Architecture

We aim to integrate frequency information into spatial-temporal networks to effectively promote detection performance for MISTD. The overall workflow of our Tridos is presented in Fig. 2. In our pipeline, we randomly sample a collection of consecutive frames $I_c = \{I_1, I_2, \dots, I_t\}$ from infrared video with a time window size of $T = t$ as input. I_t is the keyframe that needs to be detected, and the other ones are reference frames to provide context information. Then, we feed each frame into feature extractors with shared weights to obtain multi-frame features $F_c = \{F_1, F_2, \dots, F_t\} \in \mathbb{R}^{T \times C \times H \times W}$, where C , H and W indicate the channel, height and width of feature matrix, respectively. Specifically, we adopt a CSPDarknet [35] pre-trained on the COCO [36] dataset as the backbone. We design three branches to realize

the strategy of triple-domain feature learning with frequency-aware memory enhancement through memory-enhanced spatial relationship module (MSRM), temporal dynamic encoding module (TDEM), and local-global frequency-aware module (LGFm). The residual compensation unit (RCU) aims to eliminate the possible feature mismatches across different domains while fusing and enhancing different domain features. Then, the adequately interacted spatio-temporal-frequency features F_{stf} are delivered to the detection head to obtain the final results.

The MSRM receives multi-frame features F_c as input and generates the memory-enhanced spatial features F_S . Similarly, we introduce TDEM to extract target motion features F_T by employing differential learning and residual enhancing between neighboring frames. For using both the location and motion information of targets, we concatenate the spatial features F_S and temporal features F_T to capture the spatial-temporal features F_{st} , as follows:

$$F_{st} = Conv(Concat[F_S, F_T]) \quad (1)$$

where $Conv$ denotes a 3×3 convolutional layer, batch normalization and SiLU activation function. Inspired by the Fourier Transform, we transform the collection of multi-frame features F_c into frequency domain. The LGFM is proposed for modeling the local-global variation of targets in the frequency domain, enhancing target representation with different views.

$$F_{lf}, F_{gf} = LGFM(F_c) \quad (2)$$

where F_{lf} and F_{gf} are local and global features in frequency domain, respectively. Then, F_{lf} , F_{gf} and F_{st} are fed into the carefully designed RCUs to realize feature interaction and alleviate the mismatches in different domain features. The calculation process is as follows:

$$\begin{cases} F_{stf_1} = RCU_1(F_{lf}, F_{st}) \\ F_{stf_2} = RCU_2(F_{gf}, F_{st}) \\ F_{stf} = RCU_3(F_{stf_1}, F_{stf_2}) \end{cases} \quad (3)$$

After that, we obtain the compensated enhanced spatial-temporal-frequency features F_{stf} . Finally, the final detection results are acquired by the decoupled detection head of YOLOX [35] and non-maximal suppression.

B. Memory-enhanced Spatial Relationship Module

Spatial relationship modeling is essential for accurate target location prediction and tracking. Previous methods directly fuse multi-frame spatial features via concatenation [29] or multi-layer convolution [30]. They seldom consider the keyframe's global context information and the spatial dependencies between neighboring frames. To solve this, we propose the MSRM, as shown in Fig. 2. In this module, the nonlocal attention block (NAB) is introduced to obtain the long-distance dependencies between pixels in different time steps. When tracking moving targets, humans can recognize targets more accurately and extract the target's spatial relationship by comparing and inferring the features between reference frames and the keyframe. Therefore, inspired by the human visual system, we devise the memory enhancement unit (MEU) to expand

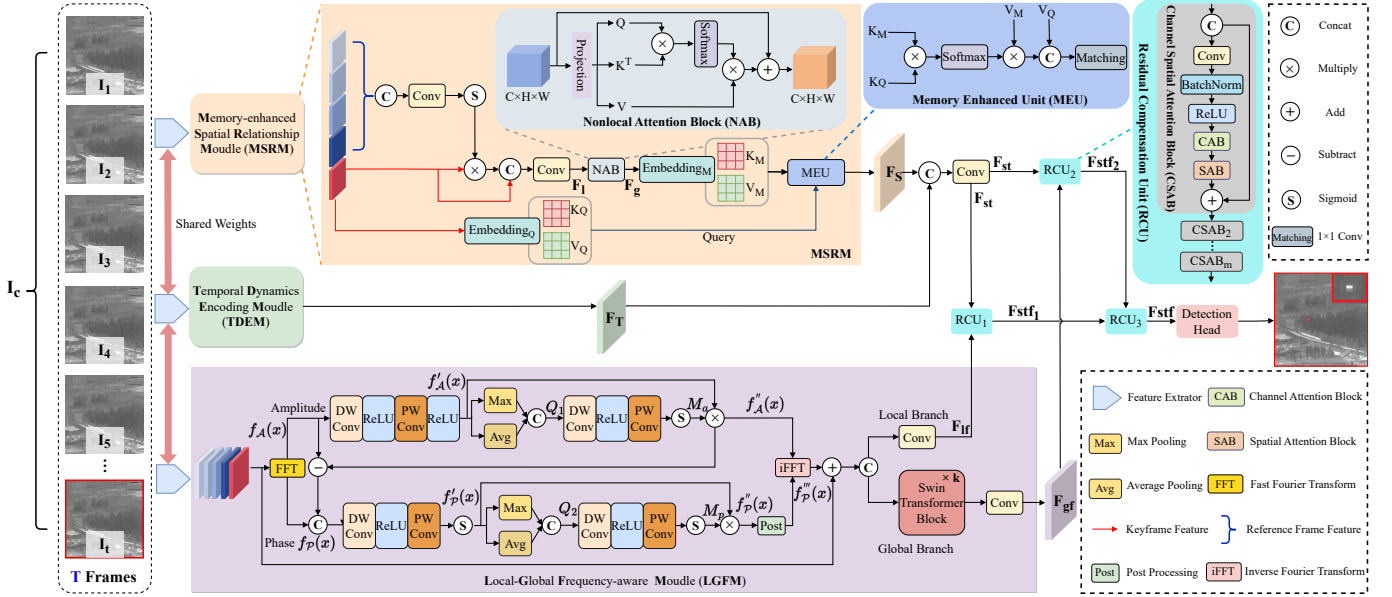


Fig. 2: Overview of the proposed framework Tridos. I_c is a collection of consecutive frames randomly sampled from infrared video. Tridos contains a backbone of shared weights to extract target features from consecutive frames, followed by the Memory-enhanced Spatial Relationship Module (MSRM), the Temporal Dynamic Encoding Module (TDEM), and the Local-Global Frequency-aware Module (LGF). Then, the features of the three branches are compensated by the Residual Compensate Units (RCU). Finally, the compensated features pass through the detection head to obtain the final results.

target features. It could fully employ multi-frame features by creating key-value pairs to better capture spatial relationships between targets.

Specifically, in MSRM, we first perform a preliminary merging of the reference frames and keyframe features through the following computational process. We assign different weights to different pixels of the reference frame.

$$\begin{aligned} \hat{F}_t &= \sigma(\text{Conv}(\text{Concat}[F_1, \dots, F_{t-1}])) \otimes F_t \\ F_l &= \text{Conv}(\text{Concat}[\hat{F}_t, F_t]) \end{aligned} \quad (4)$$

where σ denotes Sigmoid function, \otimes is matrix multiplication, \hat{F}_t is the updated keyframe features, and F_l indicates local inter-frame spatial relations.

Then, we send F_l to NAB to explore the correlation of different pixels between frames for overcoming the convolutional layer's local property, that is

$$\begin{aligned} Q, K, V &= \text{Projection}(F_l) \\ F_g &= \gamma \cdot \text{Softmax}\left(\frac{QK^T}{\sqrt{d}}\right)V + F_l \end{aligned} \quad (5)$$

where $\text{Projection}(\cdot)$ is a linear transform implemented by 1×1 convolution, γ is a hyperparameter, \sqrt{d} is the scale factor for normalization and F_g denotes inter-frame local-global spatial relations. In this way, any two pixels can interact and capture long-distance dependencies, not just limited to the local neighboring ones.

After that, we put the local-global spatial features F_g in **memory** and the keyframe features F_t as **query**, similar to the tracking mechanism of human brain. In details, we employ four distinct embedding layers to generate the corresponding

key-value pairs.

$$\begin{cases} K_Q, V_Q = f_Q(F_t) \\ K_M, V_M = f_M(F_g) \end{cases} \quad (6)$$

where $f_Q(\cdot)$ and $f_M(\cdot)$ indicate different embedding layers. Key is utilized to align the location information of targets, and value holds the high-level semantic features. In MEU, we first calculate the similarity of K_M and K_Q and normalize it through the *Softmax* function. Subsequently, the regions related to the target features are queried from V_M and concatenated with V_Q . This establishes the connection between the keyframe and reference frames and improves the target features with visual information from memory. The MEU is computed mathematically as follows:

$$\begin{aligned} M_s &= \text{Softmax}(K_M \otimes K_Q) \\ F_s &= \text{Matching}(\text{Concat}[M_s \otimes V_M, V_Q]) \end{aligned} \quad (7)$$

where M_s is the similarity matrix between K_M and K_Q , *Matching* represents 1×1 convolution and F_s denotes the local-global spatial features by memory enhancement.

C. Temporal Dynamics Encoding Module

How to extract the motion paradigm of targets is a challenging problem in MISTD. Previous methods use optical flow [20] or recurrent neural networks [32]. However, since the target is too small, the motion information between neighboring frames is not prominent. Therefore, we design TDEM, as shown in Fig. 3.

It stacks all adjacent frames' differential information within the time window to address a single difference's sparsity

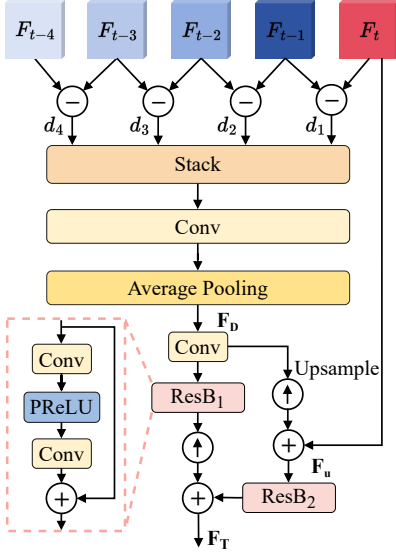


Fig. 3: The details of our proposed **Temporal Dynamic Encoding Module (TDEM)**, with a time window $T = 5$ as an example. The ResB_1 and ResB_2 are residual blocks for enhancing differential information.

problem. We further introduce residual blocks for differential information enhancement to obtain more representative motion features.

In details, TDEM dynamically encodes difference maps and propagates the local motions into the keyframe features. As shown in Fig. 3, we set the size of time window $T = 5$. Initially, we acquire continuous local motions $\mathbf{D} = [d_1, d_2, d_3, d_4]$ in sequential images by subtracting adjacent frames. Then, we use a 3×3 convolution and downsample through a average pooling with a stride of 2 to extract the motion dependencies of targets \mathbf{F}_D , which can be expressed as follows:

$$\mathbf{F}_D = \text{Avg}(\text{Conv}(\text{Stack}(d_1, d_2, d_3, d_4))) \quad (8)$$

where Avg means average pooling and Stack is the splice operation on dimension 1. We perform downsampling due to two main considerations. One is that differential information is sparse, and the motions are more prominent in low-resolution space. Another is that the pooling operation can reduce the computational cost of temporal dynamic encoding.

Moreover, we integrate motions and keyframe features to cope with the dynamic changes of targets in the temporal dimension. The motion dependencies \mathbf{F}_D restores the original size and then added to the keyframe features. Furthermore, we employ two residual blocks to boost local motions and deeply incorporate motion dependencies and target features, which can be calculated as follows:

$$\begin{aligned} \mathbf{F}_u &= \mathbf{F}_t + f_u(\text{Conv}(\mathbf{F}_D)) \\ \mathbf{F}_T &= \text{ResB}_2(\mathbf{F}_u) + f_u(\text{ResB}_1(\text{Conv}(\mathbf{F}_D))) \end{aligned} \quad (9)$$

where f_u is the upsample operation, \mathbf{F}_T denotes the motion features through temporal dynamic encoding, and ResB represents the residual block which contains two 3×3 convolutions and a PReLU activation function.

D. Local-global Frequency-aware Block

Frequency domain features can provide detailed information about targets at different frequencies and suppress image noise and interference. We aim to thoroughly explore the potential of frequency to extend target feature learning.

As shown in Fig. 2, our LGFM has two branches that can model and extract the frequency features from multiple views and levels. One is the convolution branch, which captures the local correlation and spatial structure from frequency information. The other is the swin transformer [38] branch, which models and encodes frequency features globally through a sliding window mechanism, improve the receptive field, and extract global context information.

Concretely, the Fourier transform [37] $f_{\mathcal{F}}(\cdot)$ converts each frame's features to the frequency domain space. Simply, the process can be formulated as follows for input features x :

$$f_{\mathcal{F}}(x)(u, v) = \sum_{h=0}^{H-1} \sum_{w=0}^{W-1} x(h, w) e^{-j2\pi(\frac{h}{H}u + \frac{w}{W}v)} \quad (10)$$

where u and v represent the horizontal and vertical components of frequency. H and W are the height and width of x . The frequency domain information $f_{\mathcal{F}}(x)$ can be further decomposed to the amplitude $f_{\mathcal{A}}(x)$ and the phase $f_{\mathcal{P}}(x)$, that is

$$\begin{cases} f_{\mathcal{A}}(x)(u, v) = [\mathcal{R}^2(x)(u, v) + \mathcal{I}^2(x)(u, v)]^{1/2} \\ f_{\mathcal{P}}(x)(u, v) = \arctan \left[\frac{\mathcal{I}(x)(u, v)}{\mathcal{R}(x)(u, v)} \right] \end{cases} \quad (11)$$

where $\mathcal{R}(x)$ and $\mathcal{I}(x)$ denote the real and imaginary part of $f_{\mathcal{F}}(x)$, respectively.

The motivation for decomposing the frequency features into amplitude and phase is to employ the information from these two aspects. Amplitude reflects the features' energy distribution at different frequencies, and phase comprises the position and relative relationship in the frequency domain. Initially, we process the amplitude and utilize the amplitude residuals to further extract and tune the phase. We use a 3×3 depthwise convolution $DW(\cdot)$ to independently learn spatial context information on each channel, followed by cross-channel blending with 1×1 pointwise convolution $PW(\cdot)$ aggregated pixels, as follows:

$$f'_{\mathcal{A}}(x) = \text{ReLU}(PW(\text{ReLU}(DW(f_{\mathcal{A}}(x))))) \quad (12)$$

To enhance the energy of the moving targets, we apply max pooling $\text{Max}(\cdot)$ and average pooling $\text{Avg}(\cdot)$ in the channel dimension and concatenate them. Then, the same transform as in Eq. (12) to get the amplitude attention map \mathbf{M}_a . We multiply \mathbf{M}_a with the amplitude features $f'_{\mathcal{A}}(x)$ to get the final refined amplitude features $f''_{\mathcal{A}}(x)$, which can be formulated as follows:

$$\begin{cases} \mathbf{Q}_1 = \text{Concat}[\text{Avg}(f'_{\mathcal{A}}(x)), \text{Max}(f'_{\mathcal{A}}(x))] \\ \mathbf{M}_a = \sigma(PW(\text{ReLU}(DW(\mathbf{Q}_1)))) \\ f''_{\mathcal{A}}(x) = f'_{\mathcal{A}}(x) \otimes \mathbf{M}_a \end{cases} \quad (13)$$

where $\mathbf{Q}_1 \in \mathbb{R}^{2 \times H \times W}$ and σ is *Sigmoid* function.

After that, we employ amplitude residuals $f_{\mathcal{R}}(x) = f'_{\mathcal{A}}(x) -$

$f_{\mathcal{A}}(x)$, which contain subtle amplitude variations, to modify the input and guide the phase features extraction. As for phase, we use a similar procedure as for amplitude, that is

$$\begin{cases} f'_{\mathcal{P}}(x) = \sigma(PW(ReLU(DW(Concat[f_{\mathcal{P}}(x), f_{\mathcal{R}}(x)])))) \\ \mathbf{Q}_2 = Concat[Avg(f'_{\mathcal{P}}(x)), Max(f'_{\mathcal{P}}(x))] \\ \mathbf{M}_{\mathcal{P}} = \sigma(PW(ReLU(DW(\mathbf{Q}_2)))) \\ f''_{\mathcal{P}}(x) = f'_{\mathcal{P}}(x) \otimes \mathbf{M}_{\mathcal{P}} \end{cases} \quad (14)$$

Moreover, we use post-processing to limit the phase values to $[-\pi, \pi]$, which can maintain the continuity and stability of the phase. For combining amplitude and phase, we employ the $Cos(\cdot)$ and $Sin(\cdot)$ functions to compute the real and imaginary components, as follows:

$$\begin{cases} f'''_{\mathcal{P}}(x) = 2\pi \cdot f''_{\mathcal{P}}(x) - \pi \\ \mathcal{R}'(x)(u, v) = f'_{\mathcal{A}}(x)(u, v) \cdot Cos(f'''_{\mathcal{P}}(x)(u, v)) \\ \mathcal{I}'(x)(u, v) = f'_{\mathcal{A}}(x)(u, v) \cdot Sin(f'''_{\mathcal{P}}(x)(u, v)) \end{cases} \quad (15)$$

where $x'_{\mathcal{F}} = \mathcal{R}'(x) + \mathcal{I}'(x)j$ is the integrated frequency features. Then, the inverse Fourier transformation $f_{\mathcal{F}}^{-1}(\cdot)$ is used to transform $x'_{\mathcal{F}}$ to the original domain. Suppose the input feature is x , the final output x' is obtained by adding the input x and the transformed features \hat{x} through the residuals, that is

$$\begin{aligned} \hat{x} &= f_{\mathcal{F}}^{-1}(x'_{\mathcal{F}}) \\ x' &= x + \hat{x} \end{aligned} \quad (16)$$

For the input multi-frame features collection $\mathbf{F}_{\mathcal{C}}$, we process each frame separately to get outputs $\mathbf{F}'_{\mathcal{C}} = \{\mathbf{F}'_1, \mathbf{F}'_2, \dots, \mathbf{F}'_t\} \in \mathbb{R}^{T \times C \times H \times W}$. Finally, we splice them to feed into two separate local-global branches, that is

$$\begin{aligned} \mathbf{F}_{lf} &= ConvB(Concat[\mathbf{F}'_1, \mathbf{F}'_2, \dots, \mathbf{F}'_t]) \\ \mathbf{F}_{gf} &= SwinB(Concat[\mathbf{F}'_1, \mathbf{F}'_2, \dots, \mathbf{F}'_t]) \end{aligned} \quad (17)$$

where \mathbf{F}_{lf} is the local frequency features from the convolution branch $ConvB(\cdot)$. This branch contains two 3×3 convolutions with a stride of 1, followed by batch normalization and SiLU activation function. \mathbf{F}_{gf} is the global frequency features from the swin transformer branch $SwinB(\cdot)$.

E. Residual Compensation Unit

Our scheme thoroughly explores the target's spatial, temporal, and frequency domain features. However, mismatches could happen due to the differences in the learning ways of different domain features. Therefore, we need to compensate features further to retain valuable information in different domains. With the help of RCU, the differences and commonalities between the features of different domains can be fused and enhanced, which helps to enhance the network's understanding of data and reduce the sensitivity to interference.

As shown in Fig. 2, our RCU comprises several channel spatial attention blocks (CSAB). For example, for input local frequency features \mathbf{F}_{lf} and spatial-temporal features \mathbf{F}_{st} , we first splice them in channel dimension and use a 3×3 convolution followed by batch normalization and ReLU (denoted as $Conv$) for further enhance target features. Then, we introduce a channel attention block (CAB) and a spatial attention block

(SAB) to weight features from different channels and spatial locations to adaptively focus on target significant information. Besides, feature compensation is performed by the residual branch. The residual compensation between \mathbf{F}_{lf} and \mathbf{F}_{st} can be expressed as follows:

$$\begin{cases} \mathbf{F}_r = Concat[\mathbf{F}_{lf}, \mathbf{F}_{st}] \\ CSAB = f_{SAB}(f_{CAB}(Conv(\mathbf{F}_r))) + \mathbf{F}_r \\ \mathbf{F}_{stf_1} = CASB_m(CASB_{m-1}(\dots CASB_1(\mathbf{F}_r))) \end{cases} \quad (18)$$

where m is the number of CSAB. Similarly, we perform the same operations between \mathbf{F}_{lf} and \mathbf{F}_{st} , \mathbf{F}_{stf_1} and \mathbf{F}_{stf_2} for the final refinement.

F. Dual View Regression Loss

Following the general paradigm of detection, the loss function can be expressed as

$$\mathcal{L} = \lambda_{reg} \mathcal{L}_{reg} + \lambda_{cls} \mathcal{L}_{cls} + \lambda_{obj} \mathcal{L}_{obj} \quad (19)$$

where \mathcal{L}_{reg} is a bounding box regression loss, \mathcal{L}_{cls} is a classification loss, and \mathcal{L}_{obj} is a target probability loss. λ_{reg} , λ_{cls} , and λ_{obj} are three hyper-parameters to balance portion.

For \mathcal{L}_{cls} and \mathcal{L}_{obj} , we employ sigmoid focal loss [39] to solve the problem of positive and negative sampling imbalance. In terms of \mathcal{L}_{reg} , due to the small size of the targets, using popular IoU loss could be insufficient to capture detailed information about the targets' distribution. The normalized Gaussian wasserstein distance (NWD) loss [40] can minimize the difference between target boxes by introducing a Gaussian distribution. It could efficiently model target boxes of different sizes and positions.

Therefore, we design a dual view regression loss \mathcal{L}_{dvd} to incorporate the advantages of IoU loss and NWD loss. The IoU loss assists the network in accurately localizing small targets, while the NWD loss learns the distributional properties, that is

$$\begin{cases} \mathcal{L}_{reg} = \mathcal{L}_{dvr} = \alpha \mathcal{L}_{iou} + \beta \mathcal{L}_{nwd} \\ \mathcal{L}_{iou} = 1 - IoU(B_P, B_G) \\ \mathcal{L}_{nwd} = 1 - NWD(N_P, N_G) \\ NWD(N_P, N_G) = \exp(-\frac{\sqrt{\|N_P, N_G\|_2^2}}{C}) \end{cases} \quad (20)$$

where B_P is predicted bounding box, B_G is ground truth, N_P and N_G are the Gaussian distributions for predicted boxes and ground truth, respectively. C is a constant related to datasets, and α and β are two hyper-parameters.

IV. EXPERIMENTS

A. Datasets and Evaluation Metrics

The datasets' quality, sample quantity, and scenario diversity significantly impact data-driven detection methods' performance. Currently, there are few datasets [15], [42] for MISTD. These ones are intended for aerial-based applications and aim at airborne, not ground-based vehicle targets. Thus, we reorganize an additional MISTD dataset, ITSdT-15K, to improve the quality, quantity, and diversity of infrared multi-frame datasets. The raw infrared images are from this public repository [34]. The targets in these images are moving vehicles captured by UAV infrared cameras, which are small, dim and poorly

TABLE I: Quantitative comparison results of different state-of-the-art methods on three datasets. The best and second best results are highlighted in red and blue, respectively.

Scheme	Methods	Publication	DAUB				ITSDDT-15K				IRDST			
			mAP ₅₀	Precision	Recall	F1	mAP ₅₀	Precision	Recall	F1	mAP ₅₀	Precision	Recall	F1
Model-driven	MaxMean [2]	SPIE 1999	10.71	20.38	53.87	29.57	0.87	10.85	8.74	9.68	0.01	0.28	1.48	0.47
	TopHat [1]	IPT 2006	16.99	21.69	79.83	34.11	11.61	27.21	43.07	33.35	1.81	18.22	10.60	13.40
	RLCM [4]	IEEE TGRS 2013	0.02	0.27	5.21	0.51	4.62	15.38	30.76	20.50	1.58	16.28	9.70	12.16
	HBMLCM [5]	IEEE GRSL 2019	3.90	23.96	16.52	19.56	0.72	7.97	9.37	8.61	1.16	29.14	4.66	8.03
	PSTNN [24]	RS 2019	17.31	25.56	68.86	37.28	7.99	22.98	35.21	27.81	1.45	16.28	9.70	12.16
	WSLCM [6]	SP 2020	1.37	11.88	11.57	11.73	2.36	16.78	14.53	15.58	1.69	20.87	8.70	12.28
Data-driven	ACM [9]	WACV 2021	64.02	70.96	91.3	79.86	55.38	78.37	71.69	74.88	52.40	76.33	69.32	72.66
	RISTD [43]	IEEE GRSL 2022	81.05	83.46	98.27	90.26	60.47	85.49	71.60	77.93	66.57	84.7	79.63	82.08
	ISNet [10]	CVPR 2022	83.43	89.36	94.99	92.09	62.29	83.46	75.32	79.18	59.78	80.24	75.08	77.58
	UIUNet [17]	IEEE TIP 2022	86.41	94.46	92.03	93.23	65.15	84.07	78.39	81.13	56.38	80.95	70.29	75.25
	SANet [44]	ICASSP 2023	87.12	93.44	94.93	94.18	62.17	87.78	71.23	78.64	64.54	84.29	77.02	80.49
	AGPCNet [14]	IEEE TAES 2023	76.72	82.29	94.43	87.95	67.27	91.19	74.77	82.16	59.21	79.47	75.51	77.44
	RDIAN [15]	IEEE TGRS 2023	84.92	88.2	97.27	92.51	68.49	90.56	76.06	82.68	59.08	77.99	76.35	77.16
	DNA.Net [12]	IEEE TIP 2023	89.93	92.49	98.27	95.29	70.46	88.55	80.73	84.46	63.61	82.92	77.48	80.11
	DTUM [31]	IEEE TNNLS 2023	85.86	87.54	99.79	93.26	67.97	77.95	88.28	82.79	71.48	82.87	87.79	85.26
	SIRST5K [45]	IEEE TGRS 2024	93.31	97.78	96.93	97.35	61.52	86.95	71.32	78.36	52.28	76.12	69.07	72.42
	MSHNet [46]	CVPR 2024	85.97	93.13	93.12	93.13	60.82	89.69	68.44	77.64	63.21	82.31	77.64	79.91
	RPCANet [19]	WACV 2024	85.98	89.38	97.56	93.29	62.28	81.46	77.10	79.22	56.50	77.77	73.80	75.73
	SSTNet [32]	IEEE TGRS 2024	95.59	98.08	98.10	98.09	76.96	91.05	85.29	88.07	71.55	88.56	81.92	85.11
	Tridos (Ours)	-	97.80	99.20	99.67	99.43	80.41	90.71	90.60	90.65	73.72	84.49	89.35	86.85

defined. We remove some wrong image sequences and revise the bounding boxes. Finally, our ITSDDT-15K dataset contains 15K images, including 10K training images of 40 videos and 5K test images of 20 videos, with an image resolution of 640×480 .

The ITSDDT-15K dataset contains a variety of complex scenarios, including grass, forests, obstacles, and ground clutter. Overall, our ITSDDT-15K is adequate for evaluating the performance of different methods for MISTD. Accordingly, we employ the ITSDDT-15K and two public datasets, DAUB [42] and IRDST [15], for evaluation in our experiments. For DAUB and IRDST, we follow [32] to divide the training and test sets.

In terms of evaluation metrics, following the common practice of the target detection paradigm, we apply *Precision (%)*, *Recall (%)*, *F1 score (%)*, and *Average Precision (%)* (e.g., mAP₅₀, the average Precision with an IOU threshold 0.5), which can be formulated as

$$\begin{aligned}
 \text{Precision} &= \frac{TP}{TP + FP} \\
 \text{Recall} &= \frac{TP}{TP + FN} \\
 \text{F1} &= \frac{2 \times \text{Precision} \times \text{Recall}}{\text{Precision} + \text{Recall}}
 \end{aligned} \tag{21}$$

where TP , FP , and FN denotes the number of correct detection (True positive), false alarms (False positive), and missed detection (False negative), respectively. F1 score combines *Precision* and *Recall* to assess the detector.

B. Implementation Details

In implementation, the time window size T is set to 5. For all methods, we reshape the resolution of infrared frames to 512×512 , as fair as possible. We train our Tridos for 100 epochs with batch size 4. The initial learning rate is 0.001 and adjusts adaptively with the training epoch. Adam is employed as an optimizer with the CosineAnnealingLR scheduler and momentum 0.937. We initialize the model weights with the

normal distribution. For hyper-parameters, we set λ_{reg} , λ_{cls} , and λ_{obj} in Eq. (19) to 5, 1, and 1, respectively. The α and β in Eq. (20) are both 0.5. During model testing, the IoU threshold for non-maximum suppression is 0.65, and only predicted boxes with a confidence greater than 0.001 are retained. Regarding hardware, we conduct experiments on two Nvidia GeForce 3090 GPUs.

C. Comparison With Other Methods

We choose several representative methods for comparison, including model-driven and data-driven ones. Since most of the methods are based on pixel-level segmentation, we follow the paradigm of combined detector [32] for a fair comparison.

1) *Quantitative Comparison*: The quantitative results of different detection methods on three datasets are shown in Table I. From this table, we could have **two** obvious findings.

One is that our Tridos achieves the best performance on most evaluation metrics over three datasets, especially on mAP₅₀ and F1 score. For example, on DAUB dataset, Tridos could obtain the highest mAP₅₀ 97.80% and the highest F1 99.43%. In terms of Recall, the 99.67% by Tridos is only slightly lower than the SOTA 99.79% by SSTNet. Furthermore, on ITSDDT-15K, our Tridos still obtain the highest mAP₅₀ 80.41% and F1 90.65%, far superior to the old SOTA mAP₅₀ 76.96%, and F1 score 88.07% by SSTNet. Additionally, we also outperform the comparison methods on almost all metrics on IRDST.

The other is that our Tridos has strong robustness than other ones. Almost all methods perform better on DAUB than on ITSDDT-15K and IRDST datasets. For example, on DAUB the SSTNet achieves mAP₅₀ 95.59% and F1 98.09%, but just mAP₅₀ 76.96%, F1 88.07% on ITSDDT-15K, and mAP₅₀ 71.55%, F1 85.11% on IRDST. That could be because the ITSDDT-15K and IRDST datasets contain more complex scenes with the effects of noise and occlusion. Nevertheless, Tridos improves mAP₅₀ by 2.21% and F1 by 1.34% on DAUB. On ITSDDT-15K and IRDST, mAP₅₀ improves by 3.45% and 2.17%, respectively, and F1 improves by 2.58% and 1.74%,

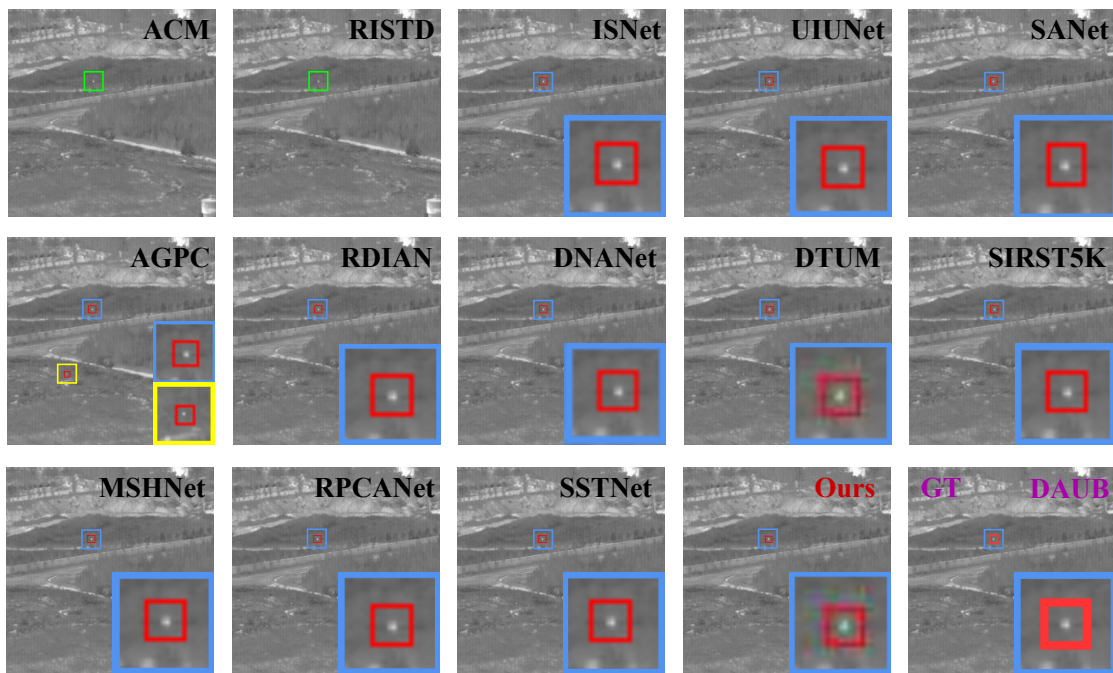


Fig. 4: The visualization comparisons of different methods on DAUB. GT is ground truth. Red, blue and green boxes represent correctly detected targets, amplified detection regions and false alarms.

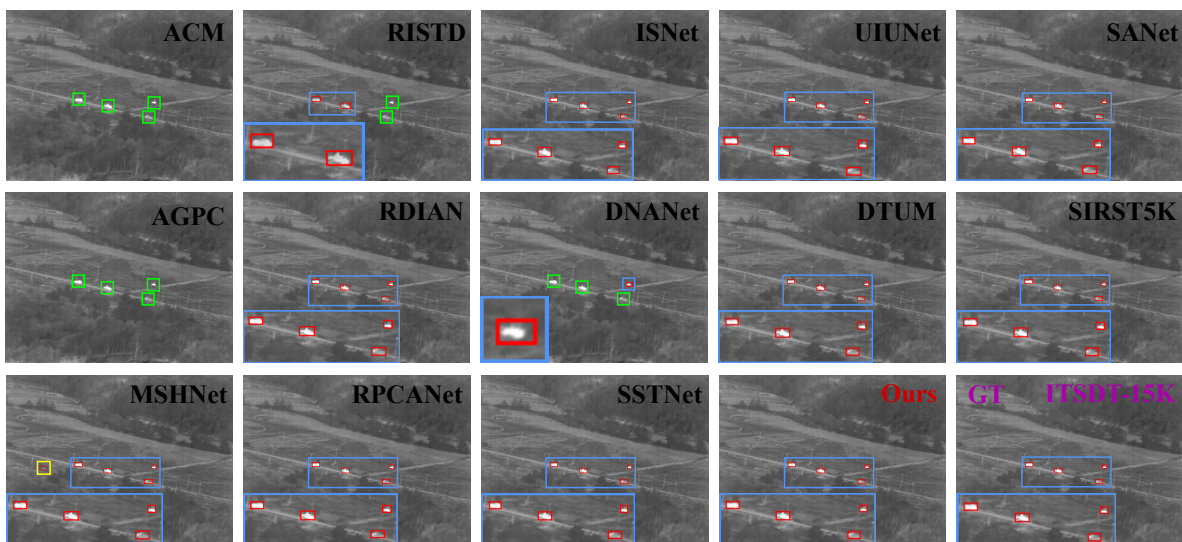


Fig. 5: The visualization comparisons of different methods on ITSDT-15K. Red, blue, and green boxes represent correctly detected targets, amplified detection regions, and false alarms.

respectively. This shows that our method is tolerant to complex scenarios. **Besides**, model-driven methods usually perform less well than data-driven methods. One possible reason is that they rely on hand-crafted features and do not have the ability to adaptively learn target features.

2) *Visual Comparison*: We present the visual comparisons of different methods in Fig. 4 - Fig. 6. It is evident that our proposed method could usually accurately detect small moving targets. In contrast, other ones often lead to miss detection or false detection.

For example, in Fig. 4, on DAUB, our Tridos precisely detects the target occluded by grass. However, ACM and

RISTD cause miss detection. AGPC incorrectly treats a bright spot as a target, producing false detection. Moreover, in Fig. 5, on ITSDT-15K, ACM, RISTD, AGPC, DNANet fail to detect all targets. MSHNet even detects five targets, causing a false detection. Meanwhile, in Fig. 6, on IRDST, ACM, RISTD, AGPC, and DNANet occur miss detection. ISNet appears false detection and it seems to have a bigger bounding box than ground truth. Besides, our Tridos produces bounding boxes with the largest similarity to ground truth. In summary, we can see that the qualitative comparison results of these visualizations correspond to the quantitative results in Table I, indicating the ascendancy of our method.

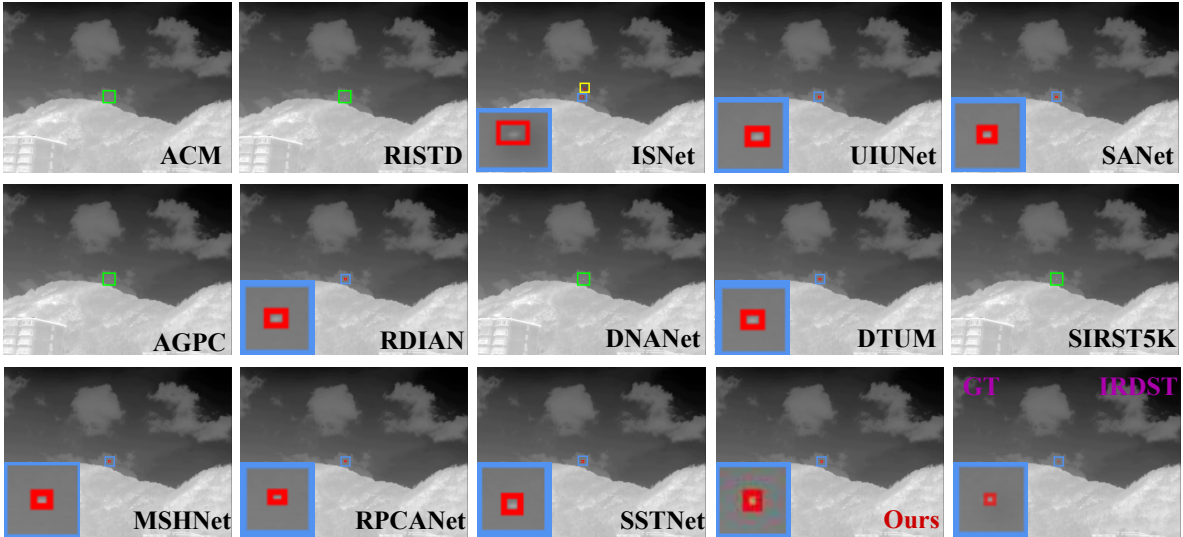


Fig. 6: The visualization comparisons of different methods on IRDST. Red, blue and green boxes represent correctly detected targets, amplified detection regions and false alarms.

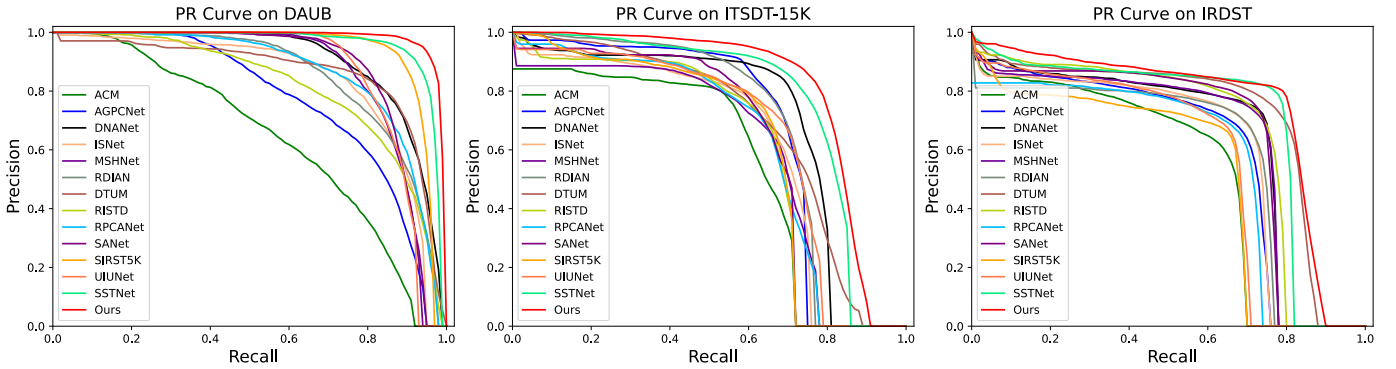


Fig. 7: PR curves of fourteen representative methods on DAUB, ITSdT-15K and IRDST.

3) *PR Curve Comparison*: To evaluate the comprehensive performance of different methods, we draw three groups of *Precision-Recall* (PR) curves on DAUB, ITSdT-15K, and IRDST, as shown in Fig. 7. By comparison, we could easily observe that our curves almost always above other ones on three datasets. The larger the area under the curve, the better the method. Therefore, the comparisons of these three groups of PR curves indicate that our Tridos has the best comprehensive performance with an optimal balance between *Precision* and *Recall*.

4) *Model Complexity Comparison*: We compare the model complexity of our Tridos with thirteen representative methods in Table II, mainly in *Params*, *GFlops*, and *FPS*. In table, we could obviously have **two** discoveries.

One is that our Tridos has a slight increase in *Params* and *GFlops*. For example, the smallest *Params* in multi-frame methods is 9.64M by DTUM. the best *GFlops* in multi-frame methods is 123.60 by SSTNet. Our Tridos has a medium *Params* 14.13M and *GFlops* 130.72. One probable reason is that SSTNet and DTUM are based on spatial-temporal domain, but our method introduces the frequency domain and needs to deal with triple domains. Overall, compared to the

TABLE II: Comparative results on the model complexity of some representative methods on ITSdT-15K. The best results are marked in bold.

Methods	Frames	mAP ₅₀ ↑	F1 ↑	Params ↓	GFlops ↓	FPS ↑
ACM [9]	1	55.38	74.88	3.04M	24.73	29.11
RISTD [43]	1	60.47	77.93	3.28M	76.28	10.21
ISNet [10]	1	62.29	79.18	3.49M	265.73	11.20
UIUNet [17]	1	65.15	81.13	53.06M	456.70	3.63
SANet [44]	1	62.17	78.64	12.40M	42.04	10.55
AGPCNet [14]	1	67.27	82.16	14.88M	366.15	4.79
RDIAN [15]	1	68.49	82.68	2.74M	50.44	20.52
DNANet [12]	1	70.46	84.46	7.22M	135.24	4.82
SIRST5K [45]	1	61.52	78.36	11.48M	182.61	7.37
MSHNet [46]	1	60.82	77.64	6.59M	69.59	18.55
RPCANet [19]	1	62.28	79.22	3.21M	382.69	15.89
DTUM [31]	5	67.97	82.79	9.64M	128.16	14.28
SSTNet [32]	5	76.96	88.07	11.95M	123.60	7.37
Ours	5	80.41	90.65	14.13M	130.72	13.71

performance gain implied in Table I, these costs are acceptable and worthwhile.

The other is that the increase in computational costs results in a middle inference speed with a *FPS* of 13.71. Besides, since multi-frame methods require processing five frames of images during inference, their *FPS* is lower than some single-

TABLE III: Ablation study on different components on two datasets, including MSRM, TDEM, LGFM and RCU. RCU(A) only use RCU₁, RCU(B) uses RCU₁ and RCU₂, and RCU(C) uses all RCUs.

Settings	MSRM	TDEM	LGFM	RCU (A)	RCU (B)	RCU (C)	DAUB				ITSDDT-15K			
							mAP ₅₀	Precision	Recall	F1	mAP ₅₀	Precision	Recall	F1
w/o All	-	-	-	-	-	-	84.43	89.73	95.45	92.50	71.95	83.43	87.35	85.34
w MSRM	✓	-	-	-	-	-	92.17	94.92	93.86	94.39	75.36	83.57	91.19	87.21
w MSRM & TDEM	✓	✓	-	-	-	-	93.73	94.51	96.24	95.37	76.77	87.03	89.72	88.35
w/o RCU	✓	✓	✓	-	-	-	95.61	96.81	97.37	97.09	78.24	85.83	92.06	88.84
w RCU(A)	✓	✓	✓	✓	-	-	95.74	97.61	97.12	97.36	79.08	89.66	89.50	89.58
w RCU(B)	✓	✓	✓	-	✓	-	96.25	98.00	99.33	98.66	79.68	89.36	90.10	89.73
w RCU(C)	✓	✓	✓	-	-	✓	97.80	99.20	99.67	99.43	80.41	90.71	90.60	90.65

frame methods, like ACM, RDIAN, MSHNet, and RPCANet. Nevertheless, our FPS is still seems higher than RISTD, ISNet, UIUNet, AGPCNet, DNANet, SIRST5K, and SSTNet.

D. Ablation Study

1) *Effects of Different Components*: We conduct four groups of ablation studies on DAUB and ITSDDT-15K to investigate the role of each component in our method, as shown in Table III - VI.

From Table III, we could have **two** findings. **One** is that each component improves network performance to some extent. For example, on DAUB, the baseline without any components just acquires 84.43% and 92.50% on mAP₅₀ and F1, respectively. MSRM could increase the mAP₅₀ from 84.43% to 92.17%, the F1 from 92.50% to 94.39%. With the assembly of TDEM, the mAP₅₀ and F1 could be further improved to 93.73% and 95.37%, respectively. Furthermore, adding frequency domain processing (w/o RCU) could provide a more distinct gain, with mAP₅₀ and F1 rising to 95.61% and 97.09%. Besides, the network performs variably with the help of different kinds of RCUs (A, B, and C). **Another** is that the best performance could be obtained by applying these components together, proving the complementary of each component. For example, when assembling all components, on DAUB, mAP₅₀ and F1 are increased to 97.80% and 99.43%. On ITSDDT-15K, mAP₅₀ and F1 are refreshed to 80.41% and 90.65%, respectively.

To explore the potential contribution of NAB and MEU in MSRM more deeply, we conduct a group of ablation studies, as shown in Table IV. In it, MEU plays an essential role in modeling inter-frame spatial relationships. For example, with the help of MEU, the mAP₅₀ and F1 on DAUB could be increased from 94.92% to 97.80%, and 98.19% to 99.43%, respectively. It implies the effectiveness of our memory mechanism. Similarly, on ITSDDT-15K, NAB could improve mAP₅₀ from 78.49% to 80.41%, and F1 from 89.08% to 90.65%. It could be attributed to the ability of NAB to capture long-distance dependencies.

TABLE IV: Ablation study on nonlocal attention block (NAB) and memory enhancement unit (MEU) of MSRM.

Settings	DAUB				ITSDDT-15K			
	mAP ₅₀	Precision	Recall	F1	mAP ₅₀	Precision	Recall	F1
MSRM w/o NAB	96.53	98.24	99.52	98.88	78.49	88.03	90.16	89.08
MSRM w/o MEU	94.92	97.57	98.81	98.19	74.05	84.91	88.74	86.78
MSRM w/o All	93.47	95.33	99.04	97.15	73.16	85.67	86.29	85.97
MSRM	97.80	99.20	99.67	99.43	80.41	90.71	90.60	90.65

From Table V, it is obvious that using two residual blocks together will get the best performance. For example, on

ITSDDT-15K, TDEM without residual blocks (TDEM w/o All) only obtain 74.05% and 86.78% on mAP₅₀ and F1. With ResB1 (TDEM w ResB1), mAP₅₀ and F1 will raise to 76.25% and 87.69%. Moreover, with all residual blocks (TDEM), mAP₅₀ and F1 will further improve 4.13% and 2.27%. This could be because ResB1 and ResB2 enhance the differential information from different perspectives, formulating more representative motion features.

TABLE V: Ablation study on two residual blocks of TDEM.

Settings	DAUB				ITSDDT-15K			
	mAP ₅₀	Precision	Recall	F1	mAP ₅₀	Precision	Recall	F1
TDEM w/o ResB1	95.49	98.08	98.87	98.48	77.21	86.58	90.25	88.38
TDEM w/o ResB2	94.45	96.24	99.42	97.80	76.25	84.57	91.05	87.69
TDEM w/o All	93.89	96.37	98.87	97.60	74.05	84.91	88.74	86.78
TDEM	97.80	99.20	99.67	99.43	80.41	90.71	90.60	90.65

Additionally, We investigate the effects of *Fourier Transform* (FT), *Conv Branch* (ConvB), and *Swin Transformer Branch* (SwinB) in Table VI.

From it, we could have **two** apparent findings. **First**, the global context acquired by the SwinB is as valuable as the local features obtained by the ConvB. For example, on DAUB, without ConvB (LGFM w/o ConvB), obtain 95.95% and 98.72%, and without SwinB achieve 95.76% and 98.39% on mAP₅₀ and F1, with almost the same decrease. **Second**, frequency transformation is a crucial strategy for detecting small targets. For example, on ITSDDT-15K, “LGFM w/o FT” only acquires 73.54% and 85.47% on mAP₅₀ and F1, even assemble with two branches. It proves that our LGFM is a successful strategy for perceiving frequency information.

TABLE VI: Ablation study of Fourier transform (FT), local branch (ConvB) and global branch (SwinB) of LGFM.

Settings	DAUB				ITSDDT-15K			
	mAP ₅₀	Precision	Recall	F1	mAP ₅₀	Precision	Recall	F1
LGFM w/o ConvB	95.95	98.61	98.94	98.72	76.73	86.04	90.35	88.14
LGFM w/o SwinB	95.76	97.52	99.27	98.39	74.77	82.01	92.37	86.88
LGFM w/o FT	94.27	97.46	97.60	97.53	73.54	86.38	84.59	85.47
LGFM w/o All	92.93	97.14	96.45	96.80	72.90	80.64	89.61	84.89
LGFM w All	97.80	99.20	99.67	99.43	80.41	90.71	90.60	90.65

2) *Effects of the Time Window Size T*: We conduct a group of experiments with different time window sizes to investigate the impact of the time window T on the detection performance of our Tridos, as shown in Fig. 8.

The time window T could provide context information for the keyframe. In Figure, we could have **two** findings. **First**, our method obtains the peak detection performance on two datasets when the time window size $T = 5$. **Second**, the proper time window size is crucial for infrared small target detection. For example, when $T \leq 3$, increasing the size of T

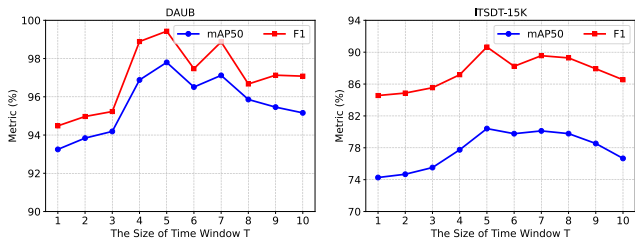


Fig. 8: The effects of the time window T on our Tridos.

results in less gain, but when $T > 3$, the detection performance improves more evidently. Furthermore, a further increase in T when $T > 5$ will lead to fluctuation or even a decrease in metrics. This could be attributed to the fact that capturing the temporal context of consecutive frames would be insufficient if the time window size is too small. Conversely, if the size is too large, there would be a risk of introducing excessive redundant messages and causing interference. Therefore, we set the time window size $T = 5$ in our final experiments.

3) *Effects of Different Detection Losses*: To validate the impacts of dual view regression loss, we further design a group of experiments, as shown in Table VII.

By comparison, our dual view regression loss gains the peak performance. For example, on DAUB, only use IoU loss realizes 96.15% and 98.56% on mAP₅₀ and F1. Nonetheless, only employing NWD loss gets 93.66% and 97.48% on mAP₅₀ and F1. One possible reason is that NWD loss improves detection accuracy by minimizing the difference in distribution between bounding boxes. However, it is sensitive to noise, which could result in inaccurate target localization. In summary, our dual view regression loss incorporates the advantages of balancing small target localization and the distribution of bounding boxes.

TABLE VII: The performance comparisons of different losses.

Settings	DAUB				ITSdT-15K			
	mAP ₅₀	Precision	Recall	F1	mAP ₅₀	Precision	Recall	F1
\mathcal{L}_{iou}	96.15	98.09	99.04	98.56	78.20	86.71	89.85	88.25
\mathcal{L}_{nwd}	93.66	96.45	98.54	97.48	73.87	82.17	84.45	83.29
\mathcal{L}_{dvr}	97.80	99.20	99.67	99.43	80.41	90.71	90.60	90.65

4) *Effects of Different Hyper-parameters*: As shown in Fig. 9, we design two groups of experiments to evaluate the effects of hyper-parameters w (the window size of the swin transformer) and c (the hidden channel numbers) on Tridos. It indicates that F1 reaches a peak on DAUB and ITSdT-15K when the window size of the swin transformer is 8. Similar to this, the highest values of F1 are obtained when the hidden channel numbers $c = 128$. Besides, we could find that Tridos’s detection performance is more sensitive to w than c . Overall, the optimal window size of the swin transformer and hidden channel numbers are 8 and 128, respectively.

5) *Comparison with Swin Transformer and YOLOX*: To further illustrate the effectiveness of our method, we compare it with a conventional swin transformer and YOLOX, as shown in Table VIII. We could find that our Tridos with frequency-aware and memory enhancement achieves evidently higher detection metrics on two datasets. For example, on ITSdT-

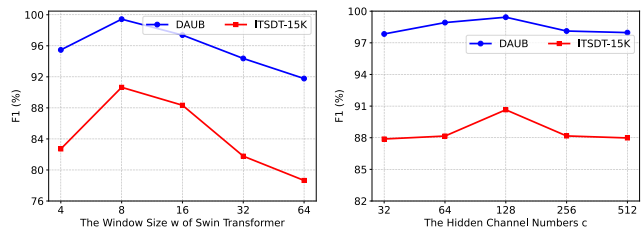


Fig. 9: The effects of hyper-parameters w and c on our Tridos.

TABLE VIII: The performance comparisons with swin transformer (SwinT) and YOLOX.

Methods	DAUB				ITSdT-15K			
	mAP ₅₀	Precision	Recall	F1	mAP ₅₀	Precision	Recall	F1
SwinT	83.40	90.46	93.45	91.93	49.93	78.56	64.30	70.72
YOLOX	85.62	90.73	94.75	92.70	72.15	84.43	86.85	85.62
Ours	97.80	99.20	99.67	99.43	80.41	90.71	90.60	90.65

15K, Tridos could acquire an mAP₅₀ 80.41%, Precision 90.71%, Recall 90.60%, and F1 90.65%, much better than swin transformer and YOLOX. This group of ablation studies further proves that our method’s superior performance is due to the strategy of triple-domain feature learning, which eliminates the effects of the swin transformer and YOLOX architecture.

V. CONCLUSION

For extending feature learning perspective, this paper proposes **Tridos** to capture the spatio-temporal-frequency features of moving infrared small targets. It enhances spatial-temporal feature representation through frequency domain and models inter-frame spatial relationships by a memory enhancement mechanism. To comprehensively evaluate different detection methods, we collect an additional MISTD dataset ITSdT-15K. The comparison experiments on DAUB, IRDST, and our own one prove the superiority of proposed Tridos to existing SOTA detection methods. Moreover, ablation studies further verify the effectiveness and merits of all elaborately-designed components in our Tridos. Although achieving expected detection performance, the utilization of frequency domain will inevitably increase network parameters and computation costs. More effective and lightweight triple-domain detection schemes could be worth further investigation in future work.

REFERENCES

- [1] X. Bai and F. Zhou, “Analysis of new top-hat transformation and the application for infrared dim small target detection,” *Pattern Recognition*, vol. 43, no. 6, pp. 2145–2156, 2010.
- [2] S. D. Deshpande, M. H. Er, R. Venkateswarlu, and P. Chan, “Max-mean and max-median filters for detection of small targets,” in *Signal and Data Processing of Small Targets 1999*, vol. 3809. SPIE, 1999, pp. 74–83.
- [3] C. P. Chen, H. Li, Y. Wei, T. Xia, and Y. Y. Tang, “A local contrast method for small infrared target detection,” *IEEE Transactions on Geoscience and Remote Sensing*, vol. 52, no. 1, pp. 574–581, 2013.
- [4] J. Han, K. Liang, B. Zhou, X. Zhu, J. Zhao, and L. Zhao, “Infrared small target detection utilizing the multiscale relative local contrast measure,” *IEEE Geoscience and Remote Sensing Letters*, vol. 15, no. 4, pp. 612–616, 2018.

- [5] J. Han, S. Moradi, I. Faramarzi, C. Liu, H. Zhang, and Q. Zhao, "A local contrast method for infrared small-target detection utilizing a tri-layer window," *IEEE Geoscience and Remote Sensing Letters*, vol. 17, no. 10, pp. 1822–1826, 2019.
- [6] J. Han, S. Moradi, I. Faramarzi, H. Zhang, Q. Zhao, X. Zhang, and N. Li, "Infrared small target detection based on the weighted strengthened local contrast measure," *IEEE Geoscience and Remote Sensing Letters*, vol. 18, no. 9, pp. 1670–1674, 2020.
- [7] C. Gao, D. Meng, Y. Yang, Y. Wang, X. Zhou, and A. G. Hauptmann, "Infrared patch-image model for small target detection in a single image," *IEEE Transactions on Image Processing*, vol. 22, no. 12, pp. 4996–5009, 2013.
- [8] X. Wang, Z. Peng, D. Kong, and Y. He, "Infrared dim and small target detection based on stable multisubspace learning in heterogeneous scene," *IEEE Transactions on Geoscience and Remote Sensing*, vol. 55, no. 10, pp. 5481–5493, 2017.
- [9] Y. Dai, Y. Wu, F. Zhou, and K. Barnard, "Asymmetric Contextual Modulation for Infrared Small Target Detection," in *2021 IEEE Winter Conference on Applications of Computer Vision (WACV)*, 2021, pp. 949–958.
- [10] M. Zhang, R. Zhang, Y. Yang, H. Bai, J. Zhang, and J. Guo, "ISNet: Shape matters for infrared small target detection," in *Proceedings of the IEEE/CVF Conference on Computer Vision and Pattern Recognition*, 2022, pp. 877–886.
- [11] H. Wang, L. Zhou, and L. Wang, "Miss detection vs. false alarm: Adversarial learning for small object segmentation in infrared images," in *Proceedings of the IEEE/CVF International Conference on Computer Vision*, 2019, pp. 8509–8518.
- [12] B. Li, C. Xiao, L. Wang, Y. Wang, Z. Lin, M. Li, W. An, and Y. Guo, "Dense nested attention network for infrared small target detection," *IEEE Transactions on Image Processing*, vol. 32, pp. 1745–1758, 2022.
- [13] Y. Dai, Y. Wu, F. Zhou, and K. Barnard, "Attentional local contrast networks for infrared small target detection," *IEEE Transactions on Geoscience and Remote Sensing*, vol. 59, no. 11, pp. 9813–9824, 2021.
- [14] T. Zhang, L. Li, S. Cao, T. Pu, and Z. Peng, "Attention-Guided Pyramid Context Networks for Detecting Infrared Small Target Under Complex Background," *IEEE Transactions on Aerospace and Electronic Systems*, vol. 59, no. 4, pp. 4250–4261, 2023.
- [15] H. Sun, J. Bai, F. Yang, and X. Bai, "Receptive-Field and Direction Induced Attention Network for Infrared Dim Small Target Detection With a Large-Scale Dataset IRDST," *IEEE Transactions on Geoscience and Remote Sensing*, vol. 61, pp. 1–13, 2023.
- [16] J. Lin, S. Li, L. Zhang, X. Yang, B. Yan, and Z. Meng, "IR-TransDet: Infrared Dim and Small Target Detection With IR-Transformer," *IEEE Transactions on Geoscience and Remote Sensing*, vol. 61, pp. 1–13, 2023.
- [17] X. Wu, D. Hong, and J. Chanussot, "UIU-Net: U-Net in U-Net for infrared small object detection," *IEEE Transactions on Image Processing*, vol. 32, pp. 364–376, 2022.
- [18] B. Yang, X. Zhang, J. Zhang, J. Luo, M. Zhou, and Y. Pi, "EFLNet: Enhancing Feature Learning Network for Infrared Small Target Detection," *IEEE Transactions on Geoscience and Remote Sensing*, vol. 62, pp. 1–11, 2024.
- [19] F. Wu, T. Zhang, L. Li, Y. Huang, and Z. Peng, "RPCANet: Deep Unfolding RPCA Based Infrared Small Target Detection," in *Proceedings of the IEEE/CVF Winter Conference on Applications of Computer Vision*, 2024, pp. 4809–4818.
- [20] C. Kwan and B. Budavari, "Enhancing small moving target detection performance in low-quality and long-range infrared videos using optical flow techniques," *Remote Sensing*, vol. 12, no. 24, p. 4024, 2020.
- [21] F. Zhao, T. Wang, S. Shao, E. Zhang, and G. Lin, "Infrared moving small-target detection via spatiotemporal consistency of trajectory points," *IEEE Geoscience and Remote Sensing Letters*, vol. 17, no. 1, pp. 122–126, 2020.
- [22] F. Wu, H. Yu, A. Liu, J. Luo, and Z. Peng, "Infrared small target detection using spatio-temporal 4d tensor train and ring unfolding," *IEEE Transactions on Geoscience and Remote Sensing*, 2023.
- [23] Y. Luo, X. Li, and S. Chen, "Feedback spatial-temporal infrared small target detection based on orthogonal subspace projection," *IEEE Transactions on Geoscience and Remote Sensing*, 2024.
- [24] G. Wang, B. Tao, X. Kong, and Z. Peng, "Infrared small target detection using nonoverlapping patch spatial-temporal tensor factorization with capped nuclear norm regularization," *IEEE Transactions on Geoscience and Remote Sensing*, vol. 60, pp. 1–17, 2021.
- [25] T. Liu, J. Yang, B. Li, C. Xiao, Y. Sun, Y. Wang, and W. An, "Nonconvex tensor low-rank approximation for infrared small target detection," *IEEE Transactions on Geoscience and Remote Sensing*, vol. 60, pp. 1–18, 2021.
- [26] F. Zhang, C. Li, and L. Shi, "Detecting and tracking dim moving point target in ir image sequence," *Infrared Physics & Technology*, vol. 46, no. 4, pp. 323–328, 2005.
- [27] X. Ren, J. Wang, T. Ma, K. Bai, M. Ge, and Y. Wang, "Infrared dim and small target detection based on three-dimensional collaborative filtering and spatial inversion modeling," *Infrared physics & technology*, vol. 101, pp. 13–24, 2019.
- [28] X. Sun, X. Liu, Z. Tang, G. Long, and Q. Yu, "Real-time visual enhancement for infrared small dim targets in video," *Infrared physics & technology*, vol. 83, pp. 217–226, 2017.
- [29] J. Du, H. Lu, L. Zhang, M. Hu, S. Chen, Y. Deng, X. Shen, and Y. Zhang, "A spatial-temporal feature-based detection framework for infrared dim small target," *IEEE Transactions on Geoscience and Remote Sensing*, vol. 60, pp. 1–12, 2021.
- [30] P. Yan, R. Hou, X. Duan, C. Yue, X. Wang, and X. Cao, "STDMA-Net: Spatio-temporal differential multiscale attention network for small moving infrared target detection," *IEEE Transactions on Geoscience and Remote Sensing*, vol. 61, pp. 1–16, 2023.
- [31] R. Li, W. An, C. Xiao, B. Li, Y. Wang, M. Li, and Y. Guo, "Direction-coded temporal u-shape module for multiframe infrared small target detection," *IEEE Transactions on Neural Networks and Learning Systems*, 2023.
- [32] S. Chen, L. Ji, J. Zhu, M. Ye, and X. Yao, "SSTNet: Sliced Spatio-Temporal Network With Cross-Slice ConvLSTM for Moving Infrared Dim-Small Target Detection," *IEEE Transactions on Geoscience and Remote Sensing*, vol. 62, pp. 1–12, 2024.
- [33] X. Tong, Z. Zuo, S. Su, J. Wei, X. Sun, P. Wu, and Z. Zhao, "ST-Trans: Spatial-Temporal Transformer for Infrared Small Target Detection in Sequential Images," *IEEE Transactions on Geoscience and Remote Sensing*, 2024.
- [34] R. Fu, H. Fan, Y. Zhu, B. Hui, Z. Zhang, P. Zhong, D. Li, S. Zhang, G. Chen, and L. Wang, "A dataset for infrared time-sensitive target detection and tracking for air-ground application," May 2022.
- [35] Z. Ge, S. Liu, F. Wang, Z. Li, and J. Sun, "YOLOX: Exceeding yolo series in 2021," *arXiv preprint arXiv:2107.08430*, 2021.
- [36] T.-Y. Lin, M. Maire, S. Belongie, J. Hays, P. Perona, D. Ramanan, P. Dollár, and C. L. Zitnick, "Microsoft coco: Common objects in context," in *Computer Vision—ECCV 2014: 13th European Conference, Zurich, Switzerland, September 6–12, 2014, Proceedings, Part V 13*. Springer, 2014, pp. 740–755.
- [37] J. W. Cooley, P. A. Lewis, and P. D. Welch, "The fast fourier transform and its applications," *IEEE Transactions on Education*, vol. 12, no. 1, pp. 27–34, 1969.
- [38] Z. Liu, J. Ning, Y. Cao, Y. Wei, Z. Zhang, S. Lin, and H. Hu, "Video swin transformer," in *Proceedings of the IEEE/CVF conference on computer vision and pattern recognition*, 2022, pp. 3202–3211.
- [39] T.-Y. Lin, P. Goyal, R. Girshick, K. He, and P. Dollár, "Focal loss for dense object detection," in *Proceedings of the IEEE International Conference on Computer Vision*, 2017, pp. 2980–2988.
- [40] C. Xu, J. Wang, W. Yang, H. Yu, L. Yu, and G.-S. Xia, "Detecting tiny objects in aerial images: A normalized wasserstein distance and a new benchmark," *ISPRS Journal of Photogrammetry and Remote Sensing*, vol. 190, pp. 79–93, 2022.
- [41] Z. Zheng, P. Wang, D. Ren, W. Liu, R. Ye, Q. Hu, and W. Zuo, "Enhancing geometric factors in model learning and inference for object detection and instance segmentation," *IEEE Transactions on Cybernetics*, vol. 52, no. 8, pp. 8574–8586, 2021.
- [42] B. Hui, Z. Song, H. Fan, P. Zhong, W. Hu, X. Zhang, J. Lin, H. Su, W. Jin, Y. Zhang, and Y. Bai, "A dataset for infrared image dim-small aircraft target detection and tracking under ground / air background," Oct. 2019.
- [43] Q. Hou, Z. Wang, F. Tan, Y. Zhao, H. Zheng, and W. Zhang, "RISTDnet: Robust infrared small target detection network," *IEEE Geoscience and Remote Sensing Letters*, vol. 19, pp. 1–5, 2021.
- [44] J. Zhu, S. Chen, L. Li, and L. Ji, "SANet: Spatial attention network with global average contrast learning for infrared small target detection," in *ICASSP 2023-2023 IEEE International Conference on Acoustics, Speech and Signal Processing (ICASSP)*. IEEE, 2023, pp. 1–5.
- [45] Y. Lu, Y. Lin, H. Wu, X. Xian, Y. Shi, and L. Lin, "SIRST-5K: Exploring Massive Negatives Synthesis with Self-supervised Learning for Robust Infrared Small Target Detection," *IEEE Transactions on Geoscience and Remote Sensing*, 2024.
- [46] Q. Liu, R. Liu, B. Zheng, H. Wang, and Y. Fu, "Infrared small target detection with scale and location sensitivity," in *Proceedings of the IEEE/CVF Computer Vision and Pattern Recognition*, 2024.

- [47] R. Kou, C. Wang, Z. Peng, Z. Zhao, Y. Chen, J. Han, F. Huang, Y. Yu, and Q. Fu, "Infrared small target segmentation networks: A survey," *Pattern Recognition*, vol. 143, p. 109788, 2023.
- [48] M. Zhao, W. Li, L. Li, J. Hu, P. Ma, and R. Tao, "Single-frame infrared small-target detection: A survey," *IEEE Geoscience and Remote Sensing Magazine*, vol. 10, no. 2, pp. 87–119, 2022.
- [49] X. Bai and Y. Bi, "Derivative entropy-based contrast measure for infrared small-target detection," *IEEE Transactions on Geoscience and Remote Sensing*, vol. 56, no. 4, pp. 2452–2466, 2018.
- [50] K. Xu, M. Qin, F. Sun, Y. Wang, Y.-K. Chen, and F. Ren, "Learning in the frequency domain," in *Proceedings of the IEEE/CVF conference on computer vision and pattern recognition*, 2020, pp. 1740–1749.
- [51] J. Li, L.-Y. Duan, X. Chen, T. Huang, and Y. Tian, "Finding the secret of image saliency in the frequency domain," *IEEE Transactions on Pattern Analysis and Machine Intelligence*, vol. 37, no. 12, pp. 2428–2440, 2015.
- [52] S. Chen, L. Ji, S. Zhu, and M. Ye, "MICPL: Motion-Inspired Cross-Pattern Learning for Small-Object Detection in Satellite Videos," *IEEE Transactions on Neural Networks and Learning Systems*, 2024.
- [53] S. Chen, J. Zhu, L. Ji, H. Pan, and Y. Xu, "Augtarget data augmentation for infrared small target detection," in *ICASSP 2023-2023 IEEE International Conference on Acoustics, Speech and Signal Processing (ICASSP)*. IEEE, 2023, pp. 1–5.